Higgs Bosons at 95 and 125 GeV in the $U(1)_X$VLFM*

Rong-Zhi Sun (孙荣智)[1,2,3] Shu-Min Zhao (赵树民)[1,2,3†] Meng-Zi Cao (曹梦姿)[1,2,3]
Song Gao (高松)[1,2,3] Xing-Xing Dong (董幸幸)[1,2,3,4‡]

[1]Department of Physics, Hebei University, Baoding 071002, China
[2]Hebei Key Laboratory of High-precision Computation and Application of Quantum Field Theory, Baoding, 071002, China
[3]Hebei Research Center of the Basic Discipline for Computational Physics, Baoding, 071002, China
[4]Departamento de Fisica and CFTP, Instituto Superior Técnico, Universidade de Lisboa, Av.Rovisco Pais 1,1049-001 Lisboa, Portugal

Abstract: We present a systematic analysis of the Higgs signal strengths at 125 GeV and 95 GeV in a non-supersymmetric $U(1)_X$ model with vector-like fermions ($U(1)_X$ VLFM). This framework extends the Standard Model (SM) by introducing an additional $U(1)_X$ gauge symmetry, three right-handed neutrinos, two singlet Higgs fields (ϕ and S), and one generation of vector-like quarks and leptons. The scalar fields mix in the neutral CP-even sector, yielding two Higgs-like states around 95 GeV and 125 GeV. We perform a χ^2 analysis that combines the Higgs signal strength measurements at 125 GeV from ATLAS and CMS, including the $\gamma\gamma$, WW^*, ZZ^*, $b\bar{b}$, and $\tau\bar{\tau}$ channels, together with the 95 GeV excesses observed in the diphoton and $b\bar{b}$ final states reported by CMS and LEP. Our results indicate that the $U(1)_X$ VLFM successfully reproduces the observed signal strengths of the 125 GeV Higgs while simultaneously explaining the 95 GeV excess. The parameters g_X, g_{YX}, v_S, v_P, and the new Yukawa couplings play a crucial role in achieving this consistency.

Keywords: Higgs signals, 95 GeV excesses, new Higgs states, non-supersymmetric extension, new physics

DOI: 10.1088/1674-1137/ae5ef8 **CSTR:**

I. INTRODUCTION

Since the discovery of a new scalar particle with a mass of about 125 GeV by the ATLAS and CMS collaborations at the Large Hadron Collider (LHC) in 2012 [1−3], its observed properties have been consistent, within current theoretical and experimental uncertainties, with expectations for the Standard Model (SM) Higgs boson. Nevertheless, such a state can also be accommodated in a wide range of theories beyond the Standard Model (BSM). Although no direct evidence of BSM physics has yet emerged at the LHC, the precision of Higgs coupling measurements and the constraints from searches for new resonances still leave substantial parameter space for new physics (NP) interpretations. Many BSM scenarios predict an extended Higgs sector, making it an essential task for LHC Run 3 and future experiments to determine whether the discovered scalar boson is part of a richer Higgs structure. Notably, these extended frameworks may feature not only heavier Higgs resonances but also lighter scalar states. The search for such light additional Higgs bosons is therefore of great importance for uncovering the underlying mechanism of electroweak symmetry breaking and for revealing possible signs of NP.

The current mass measurement of the 125 GeV Higgs boson is 125.20 ± 0.11 GeV [4]. To investigate its properties in detail and to assess whether it is the only fundamental scalar, the LHC has performed precision measurements across multiple decay channels. In particular, the ATLAS and CMS collaborations have observed the Higgs boson in various bosonic and fermionic modes [3−6], establishing its spin-parity quantum numbers and measuring its production cross sections. In the SM, the Higgs couples directly to W and Z bosons and indirectly to photons via loop effects, making the $\gamma\gamma$, WW^*, and ZZ^* channels particularly sensitive for experimental studies. The measured signal strengths in these channels are [3, 5−8]

Received 2 March 2026; Accepted 13 April 2026

* This work is supported by National Natural Science Foundation of China (NNSFC) (No.12075074), Natural Science Foundation of Hebei Province (A2023201040, A2022201022, A2022201017, A2023201041), Natural Science Foundation of Hebei Education Department (QN2022173), the Project of the China Scholarship Council (CSC) No. 202408130113. This work is also supported by Fundação para a Ciência e a Tecnologia (FCT, Portugal) through the project UID/00777/2025 (https://doi.org/10.54499/UID/00777/2025)

† E-mail: zhaosm@hbu.edu.cn
‡ E-mail: dongxx@hbu.edu.cn

$$\mu^{exp}_{\gamma\gamma}(125) = 1.10 \pm 0.06, \quad \mu^{exp}_{WW^*}(125) = 1.00 \pm 0.08,$$
$$\mu^{exp}_{ZZ^*}(125) = 1.02 \pm 0.08. \tag{1}$$

Owing to the Yukawa interactions, the Higgs boson couples most strongly to third-generation fermions, leading to dominant decays into $b\bar{b}$ and $\tau\bar{\tau}$. The corresponding measured signal strengths are reported in [3, 6, 7, 9–11].

$$\mu^{exp}_{b\bar{b}}(125) = 0.99 \pm 0.12, \quad \mu^{exp}_{\tau\bar{\tau}}(125) = 0.91 \pm 0.09. \tag{2}$$

In addition to the established Higgs boson at 125 GeV, several experimental studies have pointed to the possibility of a lighter scalar resonance near 95 GeV, renewing interest in extended Higgs sectors. Searches for additional low-mass Higgs states have been carried out at LEP [12–14], the Tevatron [15], and the LHC [16–22]. In such searches, the experimental signal strength μ is defined relative to that of a hypothetical SM Higgs boson of the same mass, even if no SM Higgs exists at that mass. Specifically, the experimental signal strengths at $m_\phi = 95.4$ GeV are:

$$\mu^{\rm exp}_{\gamma\gamma} = \frac{\sigma^{\rm exp}(gg \to \phi \to \gamma\gamma)}{\sigma^{\rm SM}(gg \to H_{\rm SM} \to \gamma\gamma)},$$
$$\mu^{\rm exp}_{b\bar{b}} = \frac{\sigma^{\rm exp}(e^+e^- \to Z\phi \to Zb\bar{b})}{\sigma^{\rm SM}(e^+e^- \to ZH_{\rm SM} \to Zb\bar{b})}, \tag{3}$$

where ϕ denotes a hypothetical BSM scalar, and $\sigma^{\rm SM}$ is the cross section for a SM-like Higgs of the same mass [23, 24].

Analyses by the CMS Collaboration in the diphoton channel at $\sqrt{s} = 8$ and 13 TeV, using datasets of 19.7 fb^{-1} and 35.9 fb^{-1}, revealed a local excess near 95.3 GeV with a significance of approximately 2.8σ [16, 17]. Using the full Run 2 dataset and improved event classification, a more recent CMS study reports a local excess at 95.4 GeV with a significance of 2.9σ [22], which is broadly compatible with ATLAS results based on 80 fb^{-1} of data [19]. The combined ATLAS+CMS signal strength can be expressed as

$$\mu^{exp}_{\gamma\gamma}(95) = 0.24^{+0.09}_{-0.08}. \tag{4}$$

Furthermore, LEP reported a 2.3σ local excess in the $e^+e^- \to Z(H \to b\bar{b})$ channel, consistent with a scalar particle with a mass of approximately 95 GeV [13]. The corresponding signal strength is

$$\mu^{exp}_{b\bar{b}}(95) = 0.117 \pm 0.057. \tag{5}$$

From a theoretical perspective, various BSM frameworks have been proposed to account for the observed excesses near 95 GeV. Previous studies [25, 26] have shown that the diphoton rate can be several times larger than the SM prediction for a scalar of the same mass in the Next-to-Minimal Supersymmetric Standard Model (NMSSM). Similarly, the Two-Higgs-Doublet Model extended with an additional real singlet (N2HDM) has been extensively explored as a possible explanation for the CMS and LEP excesses [27, 28]. Other scenarios, such as the $\mu\nu$SSM with CP conservation or violation [29–31], singlet-extended or radiative Higgs models [32], and gauge-extended frameworks like the $U(1)_X$ model [33], have also been investigated as viable possibilities.

Despite the success of the SM in describing particle interactions, it still leaves several fundamental questions unanswered, such as the nature of dark matter, the origin of neutrino masses, and the hierarchy problem. These open issues have long motivated the exploration of BSM physics. Supersymmetry (SUSY), once regarded as one of the most elegant and theoretically appealing extensions, offers a natural framework to address these problems through its fermion–boson symmetry. However, the persistent null results in supersymmetric particle searches over the past few decades have substantially reduced its experimental viability. The reported 750 GeV excess in 2015 initially generated considerable excitement as a potential signal of new physics (NP), but the 2016 data did not confirm this excess [34, 35], further decreasing overall interest in supersymmetric frameworks. Meanwhile, attention shifted toward dark matter, another compelling aspect of NP. Although significant progress has been made in dark matter searches, stringent direct-detection limits have excluded most of the viable parameter space [36, 37], leaving only narrow regions open for exploration. Consequently, interest has increasingly turned to non-supersymmetric extensions, which can offer simpler and more economical explanations. Specifically, the observation of a scalar lighter than 125 GeV would not necessarily point to a supersymmetric origin but could instead arise naturally in certain non-supersymmetric gauge extensions.

In the $U(1)_X$ VLFM, the right-handed and left-handed fields of vector-like fermions have the same transformation properties under the gauge group of the SM, allowing them to acquire gauge-invariant mass terms [38]. Consequently, they can evade constraints from Higgs production cross sections and from direct searches at the LHC. The mixing between vector-like fermions and SM fermions induces corrections to the couplings of fermions to the W, Z, and Higgs bosons [39]. As a result, the Glashow–Iliopoulos–Maiani (GIM) mechanism is generically violated, leading to flavor-changing neutral currents (FCNCs) at tree level. Moreover, vector-like fermions can introduce new CP-violating sources, contributing

to the electric dipole moments (EDMs) of leptons, quarks, and the neutron [40]. Finally, the introduced vector-like quarks can help alleviate the gauge hierarchy problem in the SM. The $U(1)_X$ VLFM accordingly offers rich phenomenology.

The remainder of this paper is organized as follows. In Sec. II A, we introduce the main components of the $U(1)_X$ VLFM, while Sec. II B presents the relevant formulae and mass matrices required for the one-loop corrections to the CP-even Higgs mass-squared matrix. In Sec. III, we derive the decay widths and corresponding signal strengths of the SM-like Higgs boson with a mass around 125 GeV, including the channels $h_2 \to \gamma\gamma$, $h_2 \to VV^*$ $(V = Z, W)$, and $h_2 \to f\bar{f}$ $(f = b, \tau)$. Sec. IV is devoted to the analysis of a lighter Higgs-like scalar near 95 GeV, where we present its dominant decay modes $h_1 \to \gamma\gamma$ and $h_1 \to b\bar{b}$ together with the corresponding signal strengths. In Sec. V, we present a numerical analysis over the relevant parameter space, and Sec. VI summarizes our main results and conclusions. For completeness, some lengthy analytical expressions are collected in Appendix A.

II. THE $U(1)_X$VLFM AND THE HIGGS SECTOR

A. The relevant content of $U(1)_X$VLFM

The gauge group of the $U(1)_X$ VLFM is $SU(3)_C \otimes SU(2)_L \otimes U(1)_Y \otimes U(1)_X$. To construct the $U(1)_X$ VLFM, the field content of the SM is extended to include three generations of right-handed neutrino fields ν_R, two singlet Higgs fields ϕ and S, and one generation of vector-like quark, lepton, and neutrino fields. The singlet Higgs fields ϕ and S are responsible for the spontaneous breaking of the additional $U(1)_X$ gauge symmetry and for generating the masses of the vector-like fermions. The inclusion of right-handed neutrinos allows light neutrino masses to be generated at tree level via the seesaw mechanism. After spontaneous symmetry breaking, the neutral CP-even components of H, ϕ, and S mix, forming a 3×3 mass-squared matrix in the scalar sector. Loop corrections from the vector-like fermions can modify the scalar mass spectrum, allowing the model to accommodate both the SM-like Higgs boson at 125 GeV and a lighter scalar state near 95 GeV.

The scalar sector of the $U(1)_X$ VLFM consists of one $SU(2)_L$ Higgs doublet H and two singlet Higgs fields ϕ and S. Their explicit forms are given below:

$$H = \begin{pmatrix} H^0 \\ H^- \end{pmatrix}, \quad H^0 = \frac{1}{\sqrt{2}}\left(v + \phi_H + i\sigma_H\right),$$
$$\phi = \frac{1}{\sqrt{2}}\left(v_P + \phi_P + i\sigma_P\right), \quad S = \frac{1}{\sqrt{2}}\left(v_S + \phi_S + i\sigma_S\right). \quad (6)$$

where v, v_P, and v_S denote the vacuum expectation values (VEVs) of the Higgs superfields H, ϕ, and S, respectively.

The two scalars play distinct roles in fermion mass generation: the VEV v_P of ϕ primarily generates the masses of vector-like fermions, while the VEV v_S of S governs the mixing between third-generation SM fermions and their vector-like counterparts. In the neutrino sector, both v_P and v_S contribute to neutrino masses via a seesaw mechanism. Therefore, two $U(1)_X$ Higgs scalars are required to obtain a realistic fermion mass spectrum and mixing structure. Introducing two singlet scalars also enlarges the parameter space, providing sufficient flexibility to simultaneously accommodate the 95 GeV and 125 GeV scalar states and to achieve a good fit to experimental data.

Although not required for anomaly cancellation, right-handed neutrinos are included to generate neutrino masses. Their contribution to the 95 GeV scalar signal is subleading, entering only through loop corrections to the scalar effective potential. Hence, their primary role is to provide a viable mechanism for light neutrino masses.

The scalar potential and Yukawa interactions relevant to the Higgs and vector-like fermion sectors can be expressed as

$$\begin{aligned}
\mathcal{L} = & -\mu_H^2 H^\dagger H - \mu_P^2|\phi|^2 - \mu_X^2|S|^2 + \lambda_H (H^\dagger H)^2 + \lambda_P|\phi|^4 + \lambda_X|S|^4 \\
& + \lambda_{HP}(H^\dagger H)|\phi|^2 + \lambda_{HX}(H^\dagger H)|S|^2 + \lambda_{PX}|S|^2|\phi|^2 \\
& - S\, d^*_{XL,k} Y^*_{XD,jk} d_{R,j} - S\, u^*_{R,j} Y_{XU,jk} u_{XL,k} - S\, e^*_{XL,k} Y^*_{XE,jk} e_{R,j} \\
& - S\, \nu^*_{R,j} Y_{XN,jk} \nu_{XL,k} - h.c. \\
& - \phi d^*_{XL,k} Y^*_{PD,jk} d_{XR,j} - \phi u^*_{XR,j} Y_{PU,jk} u_{XL,k} - \phi e^*_{XL,k} Y^*_{PE,jk} e_{XR,j} \\
& - \phi \nu^*_{XR,j} Y_{PN,jk} \nu_{XL,k} - h.c. \\
& - Y^*_{u,jk} \bar{q}_{L,k} H u_{R,j} + Y^*_{d,jk} \bar{q}_{L,k} \tilde{H} d_{R,j} + Y^*_{e,jk} \bar{l}_k \tilde{H} e_{R,j} + h.c.
\end{aligned} \quad (7)$$

The field content beyond the SM and the charge assignments of the $U(1)_X$ VLFM are presented in Table 1, where Y^Y and Y^X denote the $U(1)_Y$ and $U(1)_X$ gauge charges, respectively. As discussed in Ref. [41], the SM is free of gauge anomalies. In the extended $U(1)_X$ VLFM, a single generation of vector-like fermions is introduced to preserve this anomaly-free structure. The corresponding anomaly-cancellation conditions can be verified as follows:

1. Pure gauge anomalies involving three $SU(3)_C$ or three $SU(2)_L$ gauge bosons vanish exactly as in the SM.

2. Mixed anomalies that contain one $SU(3)_C$ or one $SU(2)_L$ gauge boson are proportional to the traces $Tr[t^a] = 0$ or $Tr[\tau^a] = 0$ and hence also vanish.

Table 1. Properties of the new particles introduced in the model

Field	$SU(3)_C$	$SU(2)_L$	$U(1)_Y$	$U(1)_X$
ϕ	1	1	0	Q_a+Q_b
S	1	1	0	Q_a
ν_R	1	1	0	0
d_{XL}	3	1	-1/3	Q_a
u_{XL}	3	1	2/3	$-Q_a$
d_{XR}	$\bar{3}$	1	1/3	Q_b
u_{XR}	$\bar{3}$	1	-2/3	$-Q_b$
e_{XL}	1	1	-1	Q_a
ν_{XL}	1	1	0	$-Q_a$
e_{XR}	1	1	1	Q_b
ν_{XR}	1	1	0	$-Q_b$

3. The mixed anomalies with one $U(1)_Y$ or $U(1)_X$ gauge boson and two $SU(3)_C$ bosons are proportional to the group-theoretical factors $Tr[t^a t^b Y^Y]=\frac{1}{2}\delta^{ab}\sum_q Y_q^Y$ or $Tr[t^a t^b Y^X]=\frac{1}{2}\delta^{ab}\sum_q Y_q^X$.

4. Similarly, the mixed anomalies involving one $U(1)_Y$ or $U(1)_X$ gauge boson and two $SU(2)_L$ bosons are proportional to $Tr[\tau^a\tau^b Y^Y]=\frac{1}{2}\delta^{ab}\sum_L Y_L^Y$ or $Tr[\tau^a\tau^b Y^X]=\frac{1}{2}\delta^{ab}\sum_L Y_L^X$.

5. The pure Abelian anomalies containing three $U(1)$ gauge bosons can be categorized into four types:

$$\begin{aligned} &Tr[Y^Y Y^Y Y^Y]=\sum_n (Y_n^Y)^3, \quad && Tr[Y^X Y^X Y^X]=\sum_n (Y_n^X)^3,\\ &Tr[Y^X Y^Y Y^Y]=\sum_n Y_n^X (Y_n^Y)^2, \quad && Tr[Y^Y Y^X Y^X]=\sum_n Y_n^Y (Y_n^X)^2. \end{aligned} \tag{8}$$

6. Mixed gravitational anomalies involving a single $U(1)$ gauge boson are proportional to $Tr[Y^Y]=\sum_n Y_n^Y$ or $Tr[Y^X]=\sum_n Y_n^X$.

Anomaly structures that do not involve the $U(1)_X$ gauge group are identical to those in the SM and are automatically consistent. For the anomaly terms associated with the additional $U(1)_X$ gauge symmetry, the inclusion of one generation of vector-like fermions ensures their complete cancellation. Therefore, all gauge and mixed gravitational anomalies are successfully canceled in the $U(1)_X$VLFM, confirming the theoretical consistency of the model.

The coexistence of two Abelian gauge groups, $U(1)_Y$ and $U(1)_X$, in the $U(1)_X$VLFM introduces a feature absent in the SM with a single $U(1)_Y$: gauge-kinetic mixing. Even if this mixing is set to zero at M_{GUT}, it can be radiatively generated through RGEs.

The covariant derivative of this model takes the general form:

$$D_\mu=\partial_\mu - i\begin{pmatrix} Y^Y, & Y^X \end{pmatrix}\begin{pmatrix} g_Y, & g'_{YX} \\ g'_{XY}, & g'_X \end{pmatrix}\begin{pmatrix} A'^Y_\mu \\ A'^X_\mu \end{pmatrix}, \tag{9}$$

we redefine the gauge fields as

$$B_\mu = g_Y A'^Y_\mu + g'_{YX} A'^X_\mu, \quad B'_\mu = g'_{XY} A'^Y_\mu + g'_X A'^X_\mu. \tag{10}$$

The gauge fields B_μ and B'_μ have canonical kinetic terms.

$$\begin{aligned} &-\frac{1}{4}B_{\mu\nu}B^{\mu\nu}-\frac{1}{4}B'_{\mu\nu}B'^{\mu\nu}.\\ &B_{\mu\nu}=\partial_\mu B_\nu-\partial_\nu B_\mu, \quad B'_{\mu\nu}=\partial'_\mu B_\nu-\partial'_\nu B_\mu. \end{aligned} \tag{11}$$

By substituting these redefinitions into the kinetic terms and expanding them, one obtains the standard form.

$$\begin{aligned} &\mathcal{L}_{\rm kin}=-\frac{1}{4}F_{\mu\nu}F^{\mu\nu}-\frac{1}{4}F'_{\mu\nu}F'^{\mu\nu}-\frac{\epsilon}{4}F_{\mu\nu}F'^{\mu\nu}\\ &F_{\mu\nu}=\partial_\mu A'^Y_\nu-\partial_\nu A'^Y_\mu, \quad F'_{\mu\nu}=\partial_\mu A'^X_\nu-\partial_\nu A'^X_\mu. \end{aligned} \tag{12}$$

where the kinetic-mixing parameter ϵ is given by:

$$\epsilon=\frac{2\left(g'_X g'_{YX}+g'_{XY}g_Y\right)}{\sqrt{\left(g'^2_X+g'^2_{XY}\right)\left(g^2_Y+g'^2_{YX}\right)}}. \tag{13}$$

This expression gives the explicit relationship between g'_{YX}, g'_{XY}, and the kinetic-mixing parameter ϵ.

A'^Y_μ and A'^X_μ denote the gauge fields associated with $U(1)_Y$ and $U(1)_X$, while Y^Y and Y^X denote the corresponding charges. In the unbroken phase, an appropriate basis rotation can be performed in gauge-field space. Introducing a transformation matrix R, the gauge-coupling matrix can be brought into an upper-triangular form:

$$\begin{pmatrix} g_Y, & g'_{YX} \\ g'_{XY}, & g'_X \end{pmatrix} R^T=\begin{pmatrix} g_1, & g_{YX} \\ 0, & g_X \end{pmatrix}. \tag{14}$$

Consequently, the $U(1)$ gauge fields are redefined as follows:

$$R\begin{pmatrix} A'^Y_\mu \\ A'^X_\mu \end{pmatrix}=\begin{pmatrix} A^Y_\mu \\ A^X_\mu \end{pmatrix}. \tag{15}$$

At tree level, the neutral gauge bosons A_μ^Y, V_μ^3, and A_μ^X mix, resulting in a nondiagonal mass matrix in the basis $(A_\mu^Y, V_\mu^3, A_\mu^X)$, which can be written as

$$\begin{pmatrix} \frac{1}{4}g_1^2v^2 & -\frac{1}{4}g_1g_2v^2 & \frac{1}{4}g_1g_{YX}v^2 \\ -\frac{1}{4}g_1g_2v^2 & \frac{1}{4}g_2^2v^2 & -\frac{1}{4}g_2g_{YX}v^2 \\ \frac{1}{4}g_1g_{YX}v^2 & -\frac{1}{4}g_2g_{YX}v^2 & \frac{1}{4}g_{YX}^2v^2+\frac{1}{4}g_X^2\xi^2 \end{pmatrix} \tag{16}$$

Here, $\xi^2 = 4(Q_a+Q_b)^2v_P^2 + 4Q_a^2v_S^2$. The diagonalization of the matrix above can be achieved through a rotation involving the weak mixing angle θ_W and an additional angle θ'_W.

$$\begin{pmatrix} \gamma_\mu \\ Z_\mu \\ Z'_\mu \end{pmatrix} = \begin{pmatrix} \cos\theta_W & \sin\theta_W & 0 \\ -\sin\theta_W\cos\theta'_W & \cos\theta_W\cos\theta'_W & \sin\theta'_W \\ \sin\theta_W\sin\theta'_W & -\cos\theta'_W\sin\theta'_W & \cos\theta'_W \end{pmatrix} \begin{pmatrix} A_\mu^Y \\ V_\mu^3 \\ A_\mu^X \end{pmatrix}. \tag{17}$$

The explicit expression for $\sin^2\theta'_W$ is given by

$$sin^2\theta'_W = \frac{1}{2} - \frac{(g_{YX}^2-g_1^2-g_2^2)v^2+g_X^2\xi^2}{2\sqrt{(g_{YX}^2+g_1^2+g_2^2)^2v^4+2g_X^2(g_{YX}^2-g_1^2-g_2^2)v^2\xi^2+g_X^4\xi^4}}. \tag{18}$$

where $\sin\theta'_W$ is of order $O(10^{-3})$ [42–44].

The new mixing angle θ'_W appears in the couplings involving Z and Z'. The exact eigenvalues of Eq. (16) are given by

$$\begin{aligned} m_\gamma^2 &= 0, \\ m_{Z,Z'}^2 &= \frac{1}{8}\Big((g_1^2+g_2^2+g_{YX}^2)v^2+g_X^2\xi^2 \\ &\quad \mp \sqrt{[(g_1^2+g_2^2+g_{YX}^2)v^2+g_X^2\xi^2]^2-4(g_1^2+g_2^2)g_X^2v^2\xi^2}\Big). \end{aligned} \tag{19}$$

In our model, the mixing between the Z boson and the TeV-scale Z' induces corrections to the Z boson mass. Expanding the exact expression in Eq. 19 in the limit $v^2 \ll \xi^2$, we obtain:

$$m_Z^2 \approx \frac{(g_1^2+g_2^2)v^2}{4} - \frac{(g_1^2+g_2^2)g_{YX}^2}{4g_X^2}\cdot\frac{v^4}{\xi^2}, \tag{20}$$

where $\xi^2 = 4(Q_a+Q_b)^2v_P^2+4Q_a^2v_S^2$, with $Q_a = Q_b = 1$.

The leading term reproduces the SM result; a further estimate yields

$$\frac{\delta m_Z^2}{m_Z^2} \sim \frac{g_{YX}^2}{g_X^2}\cdot\frac{v^2}{\xi^2} = \frac{g_{YX}^2}{g_X^2}\cdot\frac{v^2}{16v_P^2+4v_S^2} \sim O(10^{-5}). \tag{21}$$

For the W-boson mass, because the new scalar fields are singlets under $SU(2)_L$ and there are no charged scalar states (such as $H^\pm$), the W boson does not mix with them. Furthermore, electroweak symmetry breaking is dominated by the SM Higgs doublet; therefore, scalar mixing does not introduce additional corrections to the W mass. Its tree-level mass expression remains unchanged

$$m_W^2 = \frac{g_2^2v^2}{4}, \tag{22}$$

It is not affected by the mixing effects discussed above in this model.

Based on the above analysis, within the parameter regions considered in Figs. 4 and 5, the corrections to m_Z and m_W are negligible; thus, they are not included in the fit.

B. Higgs mass correction

The one-loop effective potential can be expressed as follows:

$$V_{Total} = V_{Tree} + \Delta V. \tag{23}$$

Here, V_{Tree} denotes the tree-level potential, whereas ΔV represents the one-loop correction.

The simplified Higgs potential at tree level is given as follows:

$$\begin{aligned} V_{Tree} &= \mu_H^2H^\dagger H + \mu_P^2|\phi|^2 + \mu_X^2|S|^2 - \lambda_H(H^\dagger H)^2 \\ &\quad - \lambda_P|\phi|^4 - \lambda_X|S|^4 - \lambda_{HP}(H^\dagger H)|\phi|^2 \\ &\quad - \lambda_{HX}(H^\dagger H)|S|^2 - \lambda_{PX}|S|^2|\phi|^2. \end{aligned} \tag{24}$$

We also derive the corresponding tadpole equations at tree level.

$$2\lambda_Hv^2 - 2\mu_H^2 + \lambda_{HP}v_P^2 + \lambda_{HX}v_S^2 = 0, \tag{25}$$

$$2\lambda_Xv_S^2 - 2\mu_X^2 + \lambda_{HX}v^2 + \lambda_{PX}v_P^2 = 0, \tag{26}$$

$$2\lambda_Pv_P^2 - 2\mu_P^2 + \lambda_{HP}v^2 + \lambda_{PX}v_S^2 = 0. \tag{27}$$

In addition, the tree-level mass-squared matrix for the CP-even Higgs fields (ϕ_H, ϕ_S, ϕ_P) is presented.

$$M^2_{h,tree} = \begin{pmatrix} m_{\phi_H\phi_H} & -\lambda_{HX}vv_S & -\lambda_{HP}vv_P \\ -\lambda_{HX}vv_S & m_{\phi_S\phi_S} & -\lambda_{PX}v_Pv_S \\ -\lambda_{HP}vv_P & -\lambda_{PX}v_Pv_S & m_{\phi_P\phi_P} \end{pmatrix}, \quad (28)$$

with the diagonal entries defined as

$$m_{\phi_H\phi_H} = \frac{1}{2}\left(-6\lambda_H v^2 - \lambda_{HP}v_P^2 - \lambda_{HX}v_S^2\right) + \mu_H^2, \quad (29)$$

$$m_{\phi_S\phi_S} = \frac{1}{2}\left(-6\lambda_X v_S^2 - \lambda_{HX}v^2 - \lambda_{PX}v_P^2\right) + \mu_X^2, \quad (30)$$

$$m_{\phi_P\phi_P} = \frac{1}{2}\left(-6\lambda_P v_P^2 - \lambda_{HP}v^2 - \lambda_{PX}v_S^2\right) + \mu_P^2. \quad (31)$$

Within dimensional regularization and the $\overline{\text{MS}}$ renormalization scheme in the Landau gauge, the effective Higgs potential acquires one-loop corrections, with ΔV given by the Coleman-Weinberg form [45−47]

$$\Delta V = \sum_i \frac{n_i}{64\pi^2} m_i^4(\phi_H,\phi_S,\phi_P)\left(\log\frac{m_i^2(\phi_H,\phi_S,\phi_P)}{Q^2} - \frac{3}{2}\right). \quad (32)$$

The renormalization scale Q is chosen to be of order TeV. The degrees of freedom n_i for each mass eigenstate are assigned as follows: -12 for quarks, -4 for charged leptons, -2 for neutrinos, 6 for the W boson, 3 for the Z boson, and, similarly, for the Z' boson. The explicit form of the one-loop correction to the potential reads

$$\Delta V = \sum_{f=t,b,\tau} V_f + \sum_{F=t',b',\tau'} V_F + V_{\nu'} + V_W + V_Z + V_{Z'}. \quad (33)$$

Here, V_f $(f=t,b,\tau)$ and V_F $(F=t',b',\tau')$ denote the one-loop effective potential contributions from the SM fermions and the vector-like fermions, respectively. $V_{\nu'}$ represents the contribution from the heavy neutrino sector. V_W, V_Z, and $V_{Z'}$ correspond to the contributions from the W boson, Z boson, and the Z' boson.

In the $U(1)_X$ VLFM, the fermion mass matrices arise from Yukawa interactions and are defined in the gauge-eigenstate basis. For instance, the down-type quarks are written in the bases (d_L, d_{XL}) and (d_R^*, d_{XR}^*), leading to the mass matrix

$$m_d = \begin{pmatrix} \frac{1}{\sqrt{2}}vY_d^T & 0 \\ \frac{1}{\sqrt{2}}v_S Y_{XD}^T & \frac{1}{\sqrt{2}}v_P Y_{PD}^T \end{pmatrix}. \quad (34)$$

Similarly, the up-type quarks and the charged leptons are expressed in the corresponding bases $(u_L, u_{XL}), (u_R^*, u_{XR}^*)$ and $(e_L, e_{XL}), (e_R^*, e_{XR}^*)$, respectively, with mass matrices:

$$m_u = \begin{pmatrix} \frac{1}{\sqrt{2}}vY_u^T & 0 \\ \frac{1}{\sqrt{2}}v_S Y_{XU}^T & \frac{1}{\sqrt{2}}v_P Y_{PU}^T \end{pmatrix},$$
$$m_e = \begin{pmatrix} \frac{1}{\sqrt{2}}vY_e^T & 0 \\ \frac{1}{\sqrt{2}}v_S Y_{XE}^T & \frac{1}{\sqrt{2}}v_P Y_{PE}^T \end{pmatrix}. \quad (35)$$

These Dirac-type mass matrices are diagonalized by bi-unitary transformations.

$$U_L^{f,*} m_f U_R^{f,\dagger} = m_f^{\text{diag}}, \qquad f = d,u,e, \quad (36)$$

where U_L^f and U_R^f are unitary matrices acting on the left- and right-handed fermion fields, respectively.

The neutrino sector, in the basis $(\nu_L, \nu_R^*, \nu_{XL}, \nu_{XR}^*)$, has the mass matrix:

$$m_\nu = \begin{pmatrix} 0 & \frac{1}{\sqrt{2}}vY_\nu^T & 0 & 0 \\ \frac{1}{\sqrt{2}}vY_\nu & 0 & \frac{1}{\sqrt{2}}v_S Y_{XN} & 0 \\ 0 & \frac{1}{\sqrt{2}}v_S Y_{XN}^T & 0 & \frac{1}{\sqrt{2}}v_P Y_{PN}^T \\ 0 & 0 & \frac{1}{\sqrt{2}}v_P Y_{PN} & 0 \end{pmatrix}. \quad (37)$$

Being of Majorana type, the neutrino mass matrix is diagonalized by a single unitary matrix U^V as

$$U^{V,*} m_\nu U^{V,\dagger} = m_\nu^{\text{diag}}. \quad (38)$$

The one-loop minimization conditions for the total effective potential V_{Total} within the $U(1)_X$ VLFM are given by:

$$\left\langle \frac{\partial V_{Total}}{\partial \phi_H} \right\rangle = \left\langle \frac{\partial V_{Total}}{\partial \phi_S} \right\rangle = \left\langle \frac{\partial V_{Total}}{\partial \phi_P} \right\rangle = 0, \quad (39)$$

Because the analytic forms of these conditions are cumbersome, we solve them numerically. Explicit expressions for the down-type quark sector are provided in Appendix A for reference.

The one-loop contributions to the effective potential V_{Total} give rise to radiative corrections in the mass-squared matrix of the CP-even Higgs sector.

$$M^2_{Total,h} = M^2_{Tree,h} + \Delta M^2_h, \tag{40}$$

The elements of the corrected mass-squared matrix $M^2_{Total,h,ij}$ are obtained from the second derivatives of the effective potential V_{Total}.

$$M^2_{Total,h,ij} = \left\langle \frac{\partial^2 V_{Total}}{\partial\phi_i \partial\phi_j}\Big|_{\phi_i,\phi_j=\phi_H,\phi_S,\phi_P} \right\rangle. \tag{41}$$

Diagonalization of $M^2_{Total,h}$ yields the squares of the mass eigenvalues m_{h_n} $(n=1,2,3)$, which we order as $m_{h_1} < m_{h_2} < m_{h_3}$. In this work we identify the lightest eigenstate, h_1, with the Higgs-like excess observed near 95 GeV, and the next-to-lightest eigenstate, h_2, with the SM-like Higgs boson at 125 GeV.

III. THE 125 GEV HIGGS DECAYS

At the LHC, the dominant production mode of the Higgs boson is gluon fusion. In the SM, this process proceeds at leading order (LO) via a one-loop diagram involving virtual top quarks, while subleading contributions from bottom quarks are strongly suppressed. The inclusive cross section has been computed up to next-to-next-to-leading order (NNLO) in QCD [48], which increases the LO prediction by about 80-100%. Because the gluon-fusion rate is loop-induced, it is highly sensitive to new physics (NP): any heavy particle that couples significantly to the Higgs can modify the amplitude and hence the production rate. In the $U(1)_X$ VLFM, the LO decay width for the process $h_2 \to gg$ is given by [49−54]

$$\Gamma_{NP}(h_2 \to gg) = \frac{G_F \alpha_s^2 m^3_{h_2}}{64\sqrt{2}\pi^3}\Big|\sum_{q=t,b,t',b'} g_{h_2 qq} A_{1/2}(x_q)\Big|^2, \tag{42}$$

where $x_a = m^2_{h_n}/(4m^2_a)$. The explicit expressions for the Yukawa couplings g_{huu} and g_{hdd} are given by

$$\begin{aligned} g_{h_n u_j u_j} =& -\frac{v}{m_{u_j}}\Big[-\frac{1}{\sqrt{2}}\Big(\sum_{a,b=1}^{3} Y^*_{u,ab} U^u_{R,ja} U^u_{L,jb} Z^H_{n1} \\ &+ \sum_{a}^{3} Y^*_{XU,a1} U^u_{R,ja} U^u_{L,j4} Z^H_{n2} + Y^*_{PU} U^u_{R,j4} U^u_{L,j4} Z^H_{n3}\Big)\Big], \\ &(j=1,\ldots,4), \\ g_{h_n d_j d_j} =& -\frac{v}{m_{d_j}}\Big[-\frac{1}{\sqrt{2}}\Big(\sum_{a,b=1}^{3} Y^*_{d,ab} U^d_{R,ja} U^d_{L,jb} Z^H_{n1} \\ &+ \sum_{a=1}^{3} Y^*_{XD,a1} U^d_{R,ja} U^d_{L,j4} Z^H_{n2} + Y^*_{PD} U^d_{R,j4} U^d_{L,j4} Z^H_{n3}\Big)\Big], \\ &(j=1,\ldots,4), \end{aligned} \tag{43}$$

with

$$Y^*_{XU,a1} = \begin{pmatrix} 0 \\ 0 \\ Y_{XU} \end{pmatrix} \quad \text{and} \quad Y^*_{XD,a1} = \begin{pmatrix} 0 \\ 0 \\ Y_{XD} \end{pmatrix}. \tag{44}$$

Here, $j=1,2,3$ label the SM up- and down-type quark generations, (u,c,t) and (d,s,b), respectively, while $j=4$ labels the vector-like quarks (t',b') introduced in the $U(1)_X$ VLFM extension. Z^H denotes the Higgs mixing matrix. The Yukawa couplings $Y_{XU,XD}$ and $Y_{PU,PD}$ describe the Higgs interactions with the vector-like fermions, which induce mixing with the SM quarks.

The form factor $A_{1/2}$ in Eq. (42) is defined as

$$A_{1/2}(x) = 2\left[x + (x-1)g(x)\right]/x^2, \tag{45}$$

with

$$g(x) = \begin{cases} \arcsin^2\sqrt{x}, & x \leqslant 1 \\ -\frac{1}{4}\left[\ln\frac{1+\sqrt{1-1/x}}{1-\sqrt{1-1/x}} - i\pi\right]^2, & x > 1\,. \end{cases} \tag{46}$$

The Higgs diphoton decay is mediated by loop diagrams. In the SM, the leading-order (LO) contributions arise from loops of charged gauge bosons, $W^\pm$, and top quarks. Within the $U(1)_X$-VLFM framework, additional effects are induced by the vector-like fermions t', b', and τ' that mix with the third-generation fermions. The decay width can be written as

$$\begin{aligned} \Gamma_{NP}(h_2 \to \gamma\gamma) =& \frac{G_F \alpha^2 m^3_{h_2}}{128\sqrt{2}\pi^3} \\ &\times \Big|\sum_f N_c Q_f^2 g_{h_2 ff} A_{1/2}(x_f) + g_{h_2 WW} A_1(x_W)\Big|^2, \end{aligned} \tag{47}$$

where the sum runs over the charged fermions $f = t,b,\tau,t',b',\tau'$. Here, N_c denotes the color factor ($N_c = 3$ for quarks, $N_c = 1$ for leptons), and Q_f is the corresponding electric charge.

The Higgs-fermion couplings, $g_{h_n ff}$, are obtained by diagonalizing the extended fermion mass matrices. In the leptonic sector, the coupling to the mass eigenstate l_j is

$$\begin{aligned} g_{h_n l_j l_j} =& -\frac{v}{m_{l_j}}\Big[-\frac{1}{\sqrt{2}}\Big(\sum_{a,b=1}^{3} Y^*_{e,ab} U^e_{R,ja} U^e_{L,jb} Z^H_{n1} \\ &+ \sum_{a}^{3} Y^*_{XE,a1} U^e_{R,ja} U^e_{L,j4} Z^H_{n2} + Y^*_{PE} U^e_{R,j4} U^e_{L,j4} Z^H_{n3}\Big)\Big], \\ &(j=1,\ldots,4), \end{aligned} \tag{48}$$

with

$$Y^{*}_{XE,a1} = \begin{pmatrix} 0 \\ 0 \\ Y_{XE} \end{pmatrix}. \tag{49}$$

The coupling of the Higgs boson to W bosons is determined by the Higgs mixing matrix.

$$g_{h_n WW} = Z^{H}_{n1}\,. \tag{50}$$

The loop function for spin-1 particles is given by:

$$A_1(x) = -\left[2x^2+3x+3(2x-1)g(x)\right]/x^2\,. \tag{51}$$

For the neutral CP-even Higgs boson with a mass of approximately 125 GeV, the decay modes $h_2 \to ZZ^*$ and $h_2 \to WW^*$ are kinematically allowed. After summing over all kinematically accessible final states of the off-shell vector bosons, the corresponding partial decay widths are given by [55−58].

$$\begin{aligned}\Gamma(h_2 \to WW^*) &= \frac{3e^4 m_{h_2}}{512\pi^3 s_{\rm w}^4}|g_{h_2WW}|^2 F\left(\frac{m_{\rm w}}{m_{h_2}}\right),\\ \Gamma(h_2 \to ZZ^*) &= \frac{e^4 m_{h_2}}{2048\pi^3 s_{\rm w}^4 c_{\rm w}^4}|g_{h_2ZZ}|^2\\ &\quad\times\left(7-\frac{40}{3}s_{\rm w}^2+\frac{160}{9}s_{\rm w}^4\right)F\left(\frac{m_{\rm Z}}{m_{h_2}}\right).\end{aligned} \tag{52}$$

Throughout, we adopt the abbreviations $c_{\rm w}=\cos\theta_{\rm w}$ and $s_{\rm w}=\sin\theta_{\rm w}$, with $\theta_{\rm w}$ denoting the Weinberg angle. Furthermore, e denotes the electromagnetic coupling constant.

The Higgs − Z − Z coupling is:

$$\begin{aligned}g_{h_nZZ} = \frac{v}{2m_Z^2}\Big[\frac{1}{2}\Big(v\Big(&g_1\cos\theta'_W\sin\theta_W\\ &+g_2\cos\theta_W\cos\theta'_W-g_{YX}\sin\theta'_W\Big)^2 Z^H_{n1}\\ &+\left(-2g_X\sin\theta'_W\right)^2\left(Q_a^2 v_S Z^H_{n2}+\left(Q_a+Q_b\right)^2 v_P Z^H_{n3}\right)\Big)\Big],\end{aligned} \tag{53}$$

and the form factor $F(x)$ is given as

$$\begin{aligned}F(x) = &-(1-x^2)\left(\frac{47}{2}x^2-\frac{13}{2}+\frac{1}{x^2}\right)\\ &-3(1-6x^2+4x^4)\ln x\\ &+\frac{3(1-8x^2+20x^4)}{\sqrt{4x^2-1}}\cos^{-1}\left(\frac{3x^2-1}{2x^3}\right).\end{aligned} \tag{54}$$

The partial decay width of the neutral CP-even Higgs boson of mass 125 GeV into a fermion pair is given at LO by [59, 60]

$$\Gamma_{\rm NP}(h_2 \to f\bar{f}) = N_c\frac{G_F m_f^2 m_{h_2}}{4\sqrt{2}\pi}|g_{h_2ff}|^2\left(1-\frac{4m_f^2}{m_{h_2}^2}\right)^{3/2} \quad (f=b,\tau). \tag{55}$$

Both ATLAS and CMS have observed a mild excess in Higgs-boson production with decay to the diphoton channel, relative to the SM expectation. The signal strength for a given production mode and decay channel, normalized to the corresponding SM prediction, is defined as [61]:

$$\begin{aligned}\mu^{\rm ggF}_{\gamma\gamma,VV^*}(125) &= \frac{\sigma_{\rm NP}({\rm ggF})}{\sigma_{\rm SM}({\rm ggF})}\frac{{\rm BR}_{\rm NP}(h_2\to\gamma\gamma,VV^*)}{{\rm BR}_{\rm SM}(h_2\to\gamma\gamma,VV^*)} \quad (V=Z,W),\\ \mu^{\rm VBF}_{f\bar{f}}(125) &= \frac{\sigma_{\rm NP}({\rm VBF})}{\sigma_{\rm SM}({\rm VBF})}\frac{{\rm BR}_{\rm NP}(h_2\to f\bar{f})}{{\rm BR}_{\rm SM}(h_2\to f\bar{f})} \qquad (f=b,\tau),\end{aligned} \tag{56}$$

where ggF and VBF denote gluon-gluon fusion and vector-boson fusion, respectively. When normalized to their SM values, the NP-to-SM ratios of the Higgs production cross sections are given by the corresponding ratios of the relevant partial and total decay widths.

$$\begin{aligned}\frac{\sigma_{\rm NP}({\rm ggF})}{\sigma_{\rm SM}({\rm ggF})} &\approx \frac{\Gamma_{\rm NP}(h_2\to gg)}{\Gamma_{\rm SM}(h_2\to gg)} = \frac{\Gamma^{h_2}_{\rm NP}}{\Gamma^{h_2}_{\rm SM}}\frac{\Gamma_{\rm NP}(h_2\to gg)/\Gamma^{h_2}_{\rm NP}}{\Gamma_{\rm SM}(h_2\to gg)/\Gamma^{h_2}_{\rm SM}}\\ &= \frac{\Gamma^{h_2}_{\rm NP}}{\Gamma^{h_2}_{\rm SM}}\frac{{\rm BR}_{\rm NP}(h_2\to gg)}{{\rm BR}_{\rm SM}(h_2\to gg)},\\ \frac{\sigma_{\rm NP}({\rm VBF})}{\sigma_{\rm SM}({\rm VBF})} &\approx \frac{\Gamma_{\rm NP}(h_2\to VV^*)}{\Gamma_{\rm SM}(h_2\to VV^*)} = \frac{\Gamma^{h_2}_{\rm NP}}{\Gamma^{h_2}_{\rm SM}}\frac{\Gamma_{\rm NP}(h_2\to VV^*)/\Gamma^{h_2}_{\rm NP}}{\Gamma_{\rm SM}(h_2\to VV^*)/\Gamma^{h_2}_{\rm SM}}\\ &= \frac{\Gamma^{h_2}_{\rm NP}}{\Gamma^{h_2}_{\rm SM}}\frac{{\rm BR}_{\rm NP}(h_2\to VV^*)}{{\rm BR}_{\rm SM}(h_2\to VV^*)}.\end{aligned} \tag{57}$$

Here, the total decay width of the 125 GeV Higgs boson within the NP framework is given by

$$\begin{aligned}\Gamma^{h_2}_{\rm NP} = &\sum_{f=b,\tau,c,s}\Gamma_{\rm NP}(h_2\to f\bar{f})+\sum_{V=Z,W}\Gamma_{\rm NP}(h_2\to VV^*)\\ &+\Gamma_{\rm NP}(h_2\to gg)+\Gamma_{\rm NP}(h_2\to\gamma\gamma),\end{aligned} \tag{58}$$

where contributions from rare or invisible decay channels are neglected, and $\Gamma^{h_2}_{\rm SM}$ denotes the total decay width of the SM Higgs boson. Using Eqs. (56) and (57), the signal strengths for the Higgs decay channels in the $U(1)_X$ VLFM can be expressed as

$$\mu^{\rm ggF}_{\gamma\gamma}(125) \approx \frac{\Gamma_{\rm NP}(h_2\to gg)}{\Gamma_{\rm SM}(h_2\to gg)}\frac{\Gamma_{\rm NP}(h_2\to\gamma\gamma)/\Gamma^{h_2}_{\rm NP}}{\Gamma_{\rm SM}(h_2\to\gamma\gamma)/\Gamma^{h_2}_{\rm SM}} = \frac{\Gamma^{h_2}_{\rm SM}}{\Gamma^{h_2}_{\rm NP}}\frac{\Gamma_{\rm NP}(h_2\to gg)}{\Gamma_{\rm SM}(h_2\to gg)}\frac{\Gamma_{\rm NP}(h_2\to\gamma\gamma)}{\Gamma_{\rm SM}(h_2\to\gamma\gamma)},$$

$$\mu^{\rm ggF}_{VV^*}(125) \approx \frac{\Gamma_{\rm NP}(h_2\to gg)}{\Gamma_{\rm SM}(h_2\to gg)}\frac{\Gamma_{\rm NP}(h_2\to VV^*)/\Gamma^{h_2}_{\rm NP}}{\Gamma_{\rm SM}(h_2\to VV^*)/\Gamma^{h_2}_{\rm SM}} = \frac{\Gamma^{h_2}_{\rm SM}}{\Gamma^{h_2}_{\rm NP}}\frac{\Gamma_{\rm NP}(h_2\to gg)}{\Gamma_{\rm SM}(h_2\to gg)}|g_{h_2VV}|^2,$$

$$\mu^{\rm VBF}_{f\bar f}(125) \approx \frac{\Gamma_{\rm NP}(h_2\to VV^*)}{\Gamma_{\rm SM}(h_2\to VV^*)}\frac{\Gamma_{\rm NP}(h_2\to f\bar f)/\Gamma^{h_2}_{\rm NP}}{\Gamma_{\rm SM}(h_2\to f\bar f)/\Gamma^{h_2}_{\rm SM}} = \frac{\Gamma^{h_2}_{\rm SM}}{\Gamma^{h_2}_{\rm NP}}|g_{h_2VV}|^2\,|g_{h_2ff}|^2 \qquad (V=Z,W;\ f=b,\tau), \tag{59}$$

With $\frac{\Gamma_{\rm NP}(h_2\to VV^*)}{\Gamma_{\rm SM}(h_2\to VV^*)} = |g_{h_2VV}|^2$ and $\frac{\Gamma_{\rm NP}(h_2\to f\bar f)}{\Gamma_{\rm SM}(h_2\to f\bar f)} = |g_{h_2ff}|^2$.

IV. EXCESS AT 95 GEV

The signal strengths of the 95-GeV scalar excess in the $U(1)_X$ VLFM are defined as the ratios of the corresponding production cross sections and branching ratios to their SM expectations:

$$\mu_{\gamma\gamma}(95) = \frac{\sigma_{\rm NP}(gg\to h_1)}{\sigma_{\rm SM}(gg\to h_1)}\frac{\rm BR_{NP}(h_1\to\gamma\gamma)}{\rm BR_{SM}(h_1\to\gamma\gamma)} \approx \frac{\Gamma^{h_1}_{\rm SM}}{\Gamma^{h_1}_{\rm NP}}\frac{\Gamma_{\rm NP}(h_1\to gg)}{\Gamma_{\rm SM}(h_1\to gg)}\frac{\Gamma_{\rm NP}(h_1\to\gamma\gamma)}{\Gamma_{\rm SM}(h_1\to\gamma\gamma)},$$

$$\mu_{b\bar b}(95) = \frac{\sigma_{\rm NP}(Z^*\to Zh_1)}{\sigma_{\rm SM}(Z^*\to Zh_1)}\frac{\rm BR_{NP}(h_1\to b\bar b)}{\rm BR_{SM}(h_1\to b\bar b)} \approx \frac{\Gamma^{h_1}_{\rm SM}}{\Gamma^{h_1}_{\rm NP}}\frac{\Gamma_{\rm NP}(h_1\to b\bar b)}{\Gamma_{\rm SM}(h_1\to b\bar b)}|g_{h_1ZZ}|^2, \tag{60}$$

with

$$\Gamma^{h_1}_{\rm NP} \approx \sum_{f=b,\tau,c}\Gamma_{\rm NP}(h_1\to f\bar f) + \Gamma_{\rm NP}(h_1\to gg), \tag{61}$$

In the narrow-width approximation, the signal strengths, normalized to the SM predictions, are given by Eq. 60. "NP" refers to the predictions in our BSM model ($U(1)_X$ VLFM), while "SM" refers to the hypothetical SM Higgs with the same mass [25]. $\Gamma^{h_1}_{\rm NP}$ denotes the total decay width of the 95 GeV scalar in the $U(1)_X$ VLFM, while $\Gamma^{h_1}_{\rm SM}$ corresponds to the total width of an SM Higgs boson with the same mass. The partial decay widths $\Gamma_{\rm NP(SM)}(h_1\to gg,\gamma\gamma,f\bar f)$ are evaluated analogously to Eqs. (42), (47) and (55), with h_2 replaced by h_1.

V. NUMERICAL ANALYSIS

In our numerical analysis, we assume that the lightest CP-even Higgs boson has a mass around 95 GeV, while the next-to-lightest CP-even Higgs boson is identified with the SM-like state at 125 GeV. The masses and associated signal strengths of these states are then discussed within the $U(1)_X$ VLFM framework, subject to the following phenomenological constraints:

1. The second-lightest CP-even Higgs boson h_2 is taken to be the observed Higgs boson, with mass $m_{h_2} = 125.20 \pm 0.11$ GeV as reported by the PDG [4].

2. The third-generation fermion masses are required to match their SM values after mixing with the vector-like fermions [4].

3. For the vector-like fermions in the $U(1)_X$ VLFM, we take them to be at the TeV scale [62−64].

4. Motivated by previous analyses of $U(1)_X$ extensions with vector-like fermions, we allow the Z' mass to be at the TeV scale in our numerical study, as such values have been shown to be phenomenologically viable in Refs. [65, 66].

These constraints are imposed in the parameter scan to ensure consistency with current experimental data. For the subsequent numerical analysis, we adopt the following representative benchmark scenario:

$$\begin{aligned} &Q_a = 1,\ Q_b = 1,\ Y_{XN} = 0.4,\ Y_{PN} = 0.4,\ \lambda_H = -0.12,\\ &\lambda_P = -0.003,\ \lambda_X = -0.05,\ \lambda_{HP} = -0.01,\ \lambda_{HX} = -0.03,\\ &\lambda_{PX} = -0.01,\ Y_{u_3} = 1.51Y_t,\ Y_{d_3} = 1.54Y_b,\ Y_{e_3} = 1.5Y_\tau. \end{aligned} \tag{62}$$

Here Y_t, Y_b, and Y_τ denote the Yukawa couplings of the top quark, bottom quark, and tau lepton, respectively, defined as $Y_t = \sqrt{2}m_t/v$, $Y_b = \sqrt{2}m_b/v$, and $Y_\tau = \sqrt{2}m_\tau/v$.

The benchmark points in this work are not chosen arbitrarily but are determined by the model structure and experimental constraints. In the $U(1)_X$VLFM model considered in this paper, the CP-even neutral scalar sector is described by a 3×3 mass matrix, and it must simultaneously accommodate a 125.20 ± 0.11 GeV scalar consistent with the SM Higgs and a light scalar around 95 GeV [4]. These two mass conditions impose stringent constraints on the parameter space: the parameters directly related to the scalar masses are confined to relatively narrow intervals, thereby significantly reducing their freedom.

On this basis, we further combine the Higgs signal strength measurements at 125 GeV and the excess around 95 GeV and perform a joint χ^2 fit across multiple decay channels. This procedure imposes additional experimental constraints on the parameter space, further restricting the region compatible with all observations.

In contrast, parameters that are not directly related to

the masses of these two scalars but mainly affect their decay properties have relatively broader allowed ranges and retain some degree of variability. Although the benchmark point we present corresponds to the optimal fit obtained from the χ^2 analysis, these parameters can still vary within certain ranges while maintaining a good description of the experimental data.

The benchmark point given in this work corresponds to the best-fit point obtained from the χ^2 analysis. Therefore, the apparent concentration of these parameter values mainly originates from the compression of the parameter space required to simultaneously satisfy the 95 GeV and 125 GeV experimental constraints, rather than from any ad hoc choice. In addition, the constrained parameter ranges are consistent with the typical physical scales expected in the model.

Using this benchmark, the $U(1)_X$VLFM predictions are tested against Higgs data via a χ^2 analysis, with points having χ^2 within the 3σ range of the best-fit value considered favored. The χ^2 is defined as

$$\begin{aligned}\chi^2 = \sum_i \left(\frac{\mu_i^{th}-\mu_i^{exp}}{\delta_i}\right)^2 &= \left(\frac{m_{h(125)}^{th}-m_{h(125)}^{exp}}{\delta_{m_h(125)}}\right)^2 \\ &+ \left(\frac{\mu_{b\bar{b}(95)}^{th}-\mu_{b\bar{b}(95)}^{exp}}{\delta_{\mu_{b\bar{b}}^{95}}}\right)^2 + \left(\frac{\mu_{\gamma\gamma(95)}^{th}-\mu_{\gamma\gamma(95)}^{exp}}{\delta_{\mu_{\gamma\gamma}^{95}}}\right)^2 \\ &+ \left(\frac{\mu_{\gamma\gamma(125)}^{th}-\mu_{\gamma\gamma(125)}^{exp}}{\delta_{\mu_{\gamma\gamma}^{125}}}\right)^2 + \left(\frac{\mu_{b\bar{b}(125)}^{th}-\mu_{b\bar{b}(125)}^{exp}}{\delta_{\mu_{b\bar{b}}^{125}}}\right)^2 \\ &+ \left(\frac{\mu_{ZZ^*(125)}^{th}-\mu_{ZZ^*(125)}^{exp}}{\delta_{\mu_{ZZ^*}^{125}}}\right)^2 + \left(\frac{\mu_{WW^*(125)}^{th}-\mu_{WW^*(125)}^{exp}}{\delta_{\mu_{WW^*}^{125}}}\right)^2 \\ &+ \left(\frac{\mu_{\tau\bar{\tau}(125)}^{th}-\mu_{\tau\bar{\tau}(125)}^{exp}}{\delta_{\mu_{\tau\bar{\tau}}^{125}}}\right)^2,\end{aligned} \tag{63}$$

Here, μ_i^{exp} denotes the experimental value of the corresponding observable, while μ_i^{th} represents its theoretical prediction. The term δ_i stands for the total uncertainty on the observable, including statistical and systematic experimental errors as well as theoretical uncertainties. The fit includes the 125 GeV Higgs boson mass, its signal strengths in the $\gamma\gamma$, ZZ^*, WW^*, $b\bar{b}$, and $\tau\bar{\tau}$ channels, and the potential excess at 95 GeV in the $\gamma\gamma$ and $b\bar{b}$ final states. By accounting for multiple experimental constraints from diverse physical processes, the parameter space obtained through the χ^2 analysis is more tightly constrained and reliable.

The parameters Y_{XD} and Y_{PD} represent the Yukawa couplings that link the SM-like and vector-like down-type quarks. Specifically, Y_{XD} couples the SM right-handed down quarks (d_R) to the vector-like left-handed components (d_{XL}), while Y_{PD} couples the left- and right-handed components of the vector-like quarks (d_{XL} and d_{XR}). After the singlet scalars S and ϕ_P acquire vacuum expectation values (VEVs) v_S and v_P, these couplings contribute to the mass-mixing structure of the extended quark sector, affecting both the quark masses and their interactions with the Higgs and Z' bosons. We therefore treat them as scan parameters in our analysis. Fig. 1 shows the results of the parameter scan with the benchmark set $g_X = 0.41$, $g_{YX} = -0.1$, $Y_{PU} = 0.41$, $Y_{XU} = 0.49$, $Y_{PE} = 0.32$, $Y_{XE} = 0.46$, $v_S = 1600$ GeV, and $v_P = 1900$ GeV. The scan ranges are $0 < Y_{XD} < 0.8$ and $0.1 < Y_{PD} < 0.6$. The best-fit point ($\chi^2_{\rm min} = 3.83$) is indicated by a black dot, and the 1σ, 2σ, and 3σ confidence regions are represented by ■, ♦, and ▲, respectively.

As shown in Fig. 1(a), the allowed region in the (Y_{XD}, Y_{PD}) plane forms a narrow arc-shaped band, indicating a strong correlation between the two parameters. The viable points cluster in the ranges $Y_{XD} \sim 0.30$-0.47 and $Y_{PD} \sim 0.15$-0.30, with the best-fit point at approximately (0.391, 0.310). The 1σ (■) region lies along the outer side of the arc and is somewhat shorter, while the 2σ (♦) and 3σ (▲) regions lie inward along the same trajectory and cover progressively larger portions. Within this correlated region, smaller χ^2 values are more frequently found at relatively larger Y_{PD}, indicating a mild preference for larger Y_{PD}.

In Fig. 1(b), the points form a narrow, descending band, revealing a clear anticorrelation between $\mu(h_{125})_{WW^*}$ and $\mu(h_{125})_{b\bar{b}}$. The lowest-χ^2 points are shown as ■, transitioning to ♦ and then ▲ toward the band edges. This pattern implies that when one signal strength increases, the other must decrease accordingly. As a result, they cannot vary independently and are strongly constrained by precise Higgs measurements.

In Fig. 1(c), a diagonal band of allowed points is observed, indicating a clear positive correlation between the two Higgs masses. As m_{h_1} increases from about 94.1 to 94.9 GeV, m_{h_2} rises in parallel from roughly 125.1 to 125.6 GeV. The band is relatively broad, suggesting that both masses can shift together within a finite range while remaining consistent with the constraints. The best-fit point, indicated by the black dot, is located at approximately $m_{h_1} = 94.19$ GeV and $m_{h_2} = 125.20$ GeV, a result that is particularly significant, as it simultaneously aligns with the 95 GeV scalar excess and the observed 125 GeV Higgs boson.

The parameter Y_{XE} governs the mixing between the vector-like lepton and the tau lepton, while Y_{PE} primarily determines the mass of the vector-like lepton. Fig. 2 presents the χ^2 distribution obtained from a scan over Y_{XE} and Y_{PE} within $0 < Y_{XE} < 0.8$ and $0.1 < Y_{PE} < 0.6$, using the benchmark parameters $g_X = 0.41$, $g_{YX} = -0.1$, $Y_{PU} = 0.41$, $Y_{XU} = 0.49$, $Y_{PD} = 0.3$, $Y_{XD} = 0.41$, $v_S = 1600$ GeV, and $v_P = 1900$ GeV. The best-fit point ($\chi^2_{\rm min} = 4.0$, •) is indicated, and the 1σ (■), 1-2σ (♦), and 2-3σ (▲) regions highlight the parameter space favored

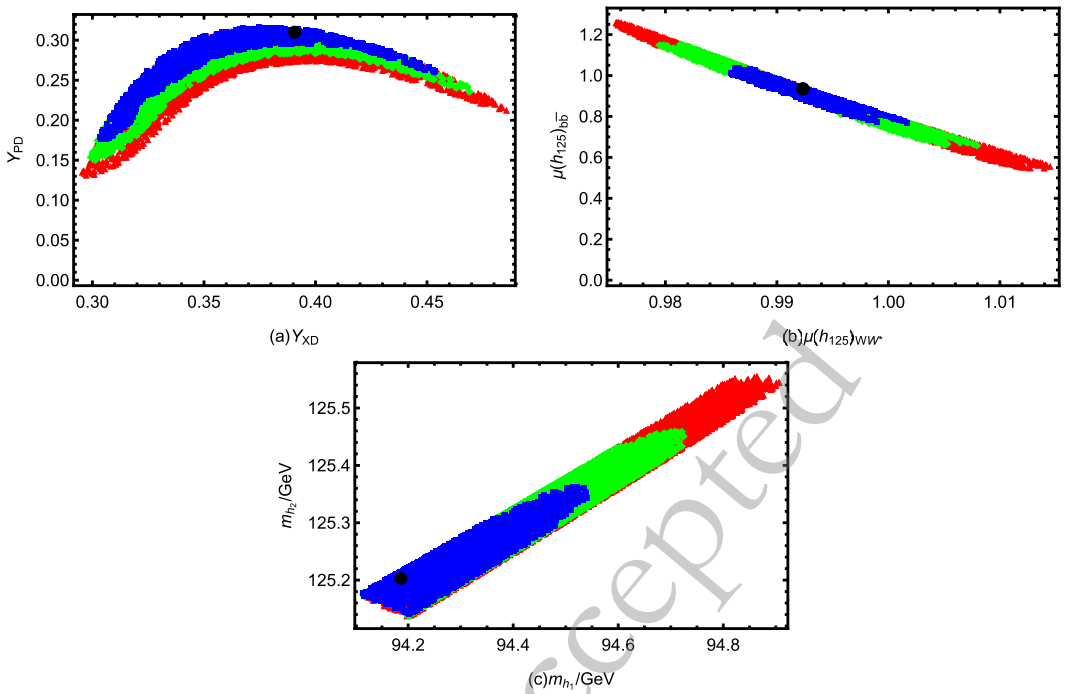

Fig. 1. The symbols denote the χ^2 confidence regions as follows: • denotes the best-fit point ($\chi^2_{\rm min} = 3.83$); ■ denotes the 1σ region ($\chi^2 \leq 6.13$); ♦ denotes the 1-2σ region ($6.13 < \chi^2 \leq 10.01$); and ▲ denotes the 2-3σ region ($10.01 < \chi^2 \leq 15.66$).

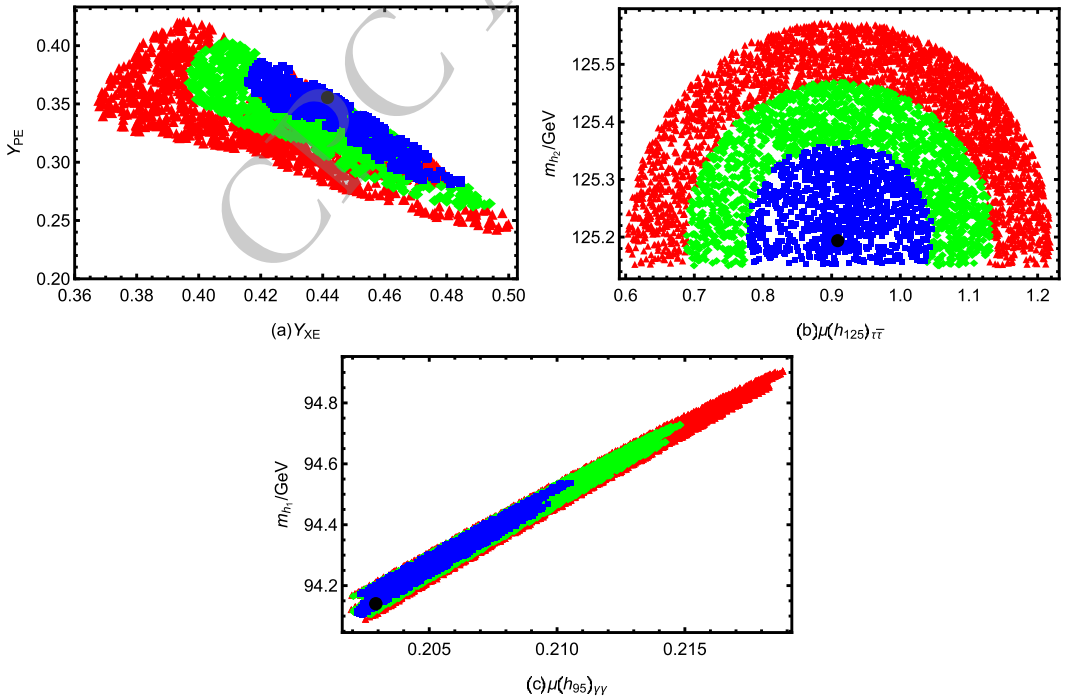

Fig. 2. The symbols indicate the χ^2 confidence regions: • marks the best-fit point ($\chi^2_{\rm min} = 4.0$); ■ denotes the 1σ region ($\chi^2 \leq 6.3$); ♦ indicates the 1-2σ region ($6.3 < \chi^2 \leq 10.18$); and ▲ corresponds to the 2-3σ region ($10.18 < \chi^2 \leq 15.83$).

by the fit.

In Fig. 2(a), the allowed parameter space forms a tilted, wedge-like strip extending from the upper left to the lower right of the (Y_{XE}, Y_{PE}) plane, indicating a clear inverse correlation between the two couplings. The best-fit point lies within the compact 1σ region, while the 2σ and 3σ regions expand outward along the same orientation. This stratified pattern suggests that only correlated variations in Y_{XE} and Y_{PE} are compatible with the Higgs signal strength measurements, thereby imposing strin-

gent constraints on the Yukawa structure in the lepton sector.

In Fig. 2(b), we map the viable points in the plane spanned by the $\tau\bar{\tau}$ signal strength of h_{125} and the mass of the 125 GeV Higgs boson. The results exhibit a series of nested, semicircular layers centered on $m_{h_2} \simeq 125.2$ GeV, reflecting the strong experimental preference for a Higgs-boson mass consistent with that of the SM-like Higgs boson. The 1σ region (■) is tightly concentrated near this central value, while the 2σ (♦) and 3σ (▲) regions form successive shells that extend outward, indicating a gradual deterioration of the fit quality as the mass departs from the preferred point. The best-fit point, marked by the black dot at $(\mu(h_{125})_{\tau\bar{\tau}}, m_{h_2}) \simeq (0.91, 125.19\ \text{GeV})$, lies extremely close to the PDG world average of $m_{h_2} = 125.20 \pm 0.11$ GeV, demonstrating excellent agreement between the model prediction and current Higgs measurements. This pattern indicates that, with the Higgs mass fixed near its measured value, the $\tau\bar{\tau}$ signal strength can vary only within a very narrow range because of strong experimental constraints.

In Fig. 2(c), we show the correlation between the diphoton signal strength of the 95 GeV scalar, $\mu(h_{95})_{\gamma\gamma}$, and its mass m_{h_1}. The distribution of points forms an inclined band, indicating a positive correlation: m_{h_1} increases from approximately 94.1 GeV to 95.0 GeV as $\mu(h_{95})_{\gamma\gamma}$ increases. The global best-fit point is located at the lower boundary of this region. The symbols and their colors represent the CL, with ■ denoting the most favored region, followed by ♦ and then ▲. This correlation reflects intrinsic model constraints that link the diphoton rate and the mass of the 95 GeV scalar.

Similarly, in the up-type quark sector, the parameters Y_{XU} and Y_{PU} characterize the Yukawa interactions responsible for the coupling between the SM top quark and a vector-like fermion. They determine the strength of this interaction, thereby influencing the structure of the up-type quark mass matrix and the mixing pattern in the extended quark sector. Both parameters are included as scan variables in the numerical analysis. In Fig. 3, with $g_X = 0.41$, $g_{YX} = -0.1$, $Y_{XE} = 0.46$, $Y_{PE} = 0.32$, $Y_{XD} = 0.41$, $Y_{PD} = 0.3$, $v_S = 1600$ GeV, and $v_P = 1900$ GeV fixed, we perform a parameter scan over Y_{XU} and Y_{PU} across $0 < Y_{XU} < 0.8$ and $0.1 < Y_{PU} < 0.6$. The best-fit point is found at $\chi^2_{\text{min}} = 3.36$, while the surrounding regions correspond approximately to the 1σ ($\chi^2 \leq 5.66$), 1-2σ ($5.66 < \chi^2 \leq 9.54$), and 2-3σ ($9.54 < \chi^2 \leq 15.19$) confidence levels.

Fig. 3(a) displays the fitted parameter distribution in the (Y_{PU}, Y_{XU}) plane. The points align along a well-defined descending strip, reflecting a compensating relation between the two couplings. The global best-fit point, marked by the black dot at $(Y_{PU}, Y_{XU}) \simeq (0.420, 0.487)$, lies within the compact 1σ region, which is successively enclosed by the broader 2σ and 3σ confidence regions. This nested structure highlights the statistical hierarchy of the fit and demonstrates that Higgs observables can be satisfied only through a tightly correlated adjustment of

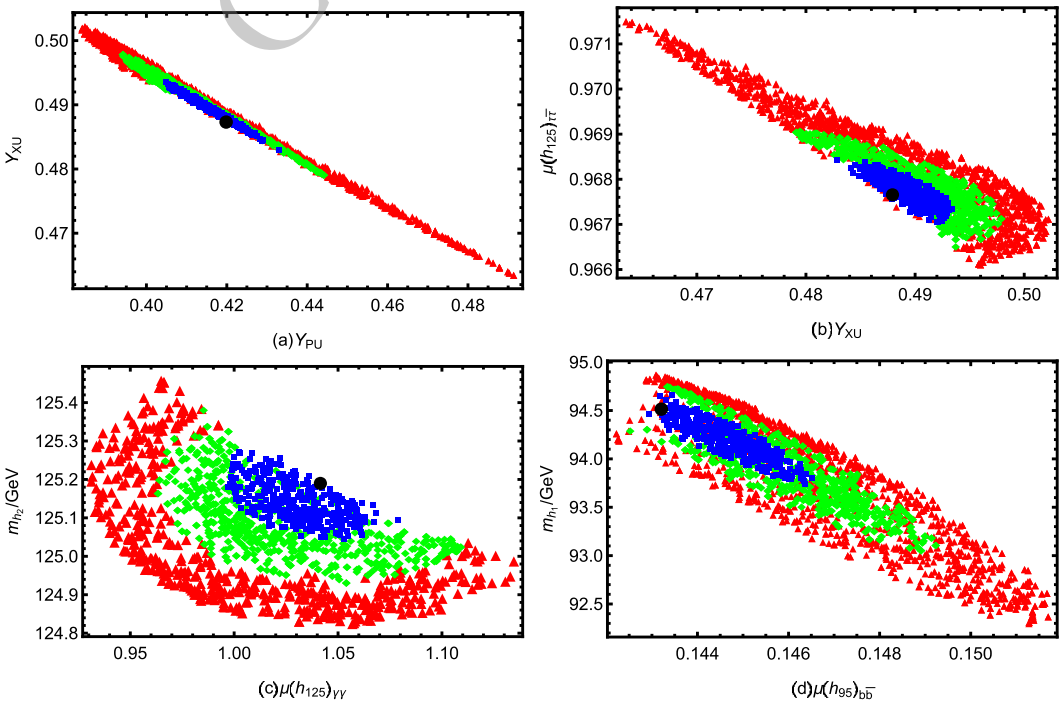

Fig. 3. The symbols denote the χ^2 confidence regions as follows: • denotes the best-fit point ($\chi^2_{\text{min}} = 3.36$); ■ denotes the 1σ region ($\chi^2 \leq 5.66$); ♦ denotes the 1-2σ region ($5.66 < \chi^2 \leq 9.54$); and ▲ denotes the 2-3σ region ($9.54 < \chi^2 \leq 15.19$).

Y_{PU} and Y_{XU}.

Fig. 3(b) shows the correlation between Y_{XU} and $\mu(h_{125})_{\tau\bar{\tau}}$. Compared with Fig. 3(a), the distribution here is noticeably broader, with the outer regions extending into a long descending tail. The best-fit point lies near the center of the innermost domain, and any deviation from this point quickly worsens the fit. This pattern indicates that, although some flexibility exists, the $\tau\bar{\tau}$ signal strength remains tightly correlated with Y_{XU}.

Fig. 3(c) presents the distribution of points in the plane of the h_{125} diphoton signal strength versus its mass ($\mu(h_{125})_{\gamma\gamma}$, m_{h_2}). The points trace a tilted, semicircular arc: m_{h_2} is constrained within a narrow range of 124.8-125.4 GeV, while $\mu(h_{125})_{\gamma\gamma}$ varies close to the SM expectation, spanning 0.95-1.10. It reveals a compact ■ core, successively surrounded by ♦ and ▲ layers that form nested semicircular envelopes, with the outer layer spanning the widest arc. The global best-fit point at $(\mu(h_{125})_{\gamma\gamma}, m_{h_2}) \simeq (1.04, 125.19\,\text{GeV})$ lies well inside the core. A mild anticorrelation emerges along the arc, with m_{h_2} decreasing slightly as $\mu(h_{125})_{\gamma\gamma}$ increases, indicating constrained joint variations rather than independent scatter.

In Fig. 3(d), the allowed points cluster into a diagonal band extending from the upper-left to the lower-right of the ($\mu(h_{95})_{b\bar{b}}$, m_{h_1}) plane. The strip exhibits a compact ■ core is enclosed by ♦ and then ▲ regions, forming a slender corridor of viable points. A clear anticorrelation is observed: larger values of $\mu(h_{95})_{b\bar{b}}$ correspond to smaller m_{h_1}, indicating that the two observables are tightly constrained by the fit. The best-fit point, $(\mu(h_{95})_{b\bar{b}}, m_{h_1}) \simeq (0.143, 94.51\,\text{GeV})$, lies near the upper boundary of the ■ core, highlighting a preference for a slightly heavier h_1 mass accompanied by a reduced $b\bar{b}$ signal strength.

In the $U(1)_X$VLFM, v_S and v_P denote the VEVs of the singlet scalars S and ϕ_P, respectively. These VEVs break the extra $U(1)_X$ gauge symmetry and generate masses for the new gauge boson Z' as well as the vector-like fermions through their Yukawa interactions. They also play an important role in determining the scalar mass spectrum. Therefore, we take v_S and v_P as key parameters in our numerical analysis. In Fig. 4, we perform an extended scan over the scalar VEVs, $1200\,\text{GeV} < v_S < 2500\,\text{GeV}$ and $1600\,\text{GeV} < v_P < 2800\,\text{GeV}$, while keeping $g_X = 0.41$, $g_{YX} = -0.1$, $Y_{XE} = 0.46$, $Y_{PE} = 0.32$, $Y_{XD} = 0.41$, $Y_{PD} = 0.3$, $Y_{XU} = 0.49$, and $Y_{PU} = 0.41$ fixed. The resulting χ^2 distribution is shown, with the best-fit point at $\chi^2_{\text{min}} = 4.39$ (•) and the 1σ, 1-2σ, and 2-3σ confidence regions indicated by ■, ♦, and ▲, respectively.

Fig. 4(a) displays the viable region in the (v_S, v_P) plane. The points align along a narrow diagonal band, revealing a strong positive correlation between the two VEVs. The distribution is coded by χ^2 using both color and shape, with a compact ■ core, surrounded by ♦, and ▲ outer layers, corresponding to increasing χ^2 values. The best-fit point, $(v_S, v_P) \simeq (1601.8, 1915.2\,\text{GeV})$, lies near the center of the innermost region, representing the most statistically favored vacuum configuration.

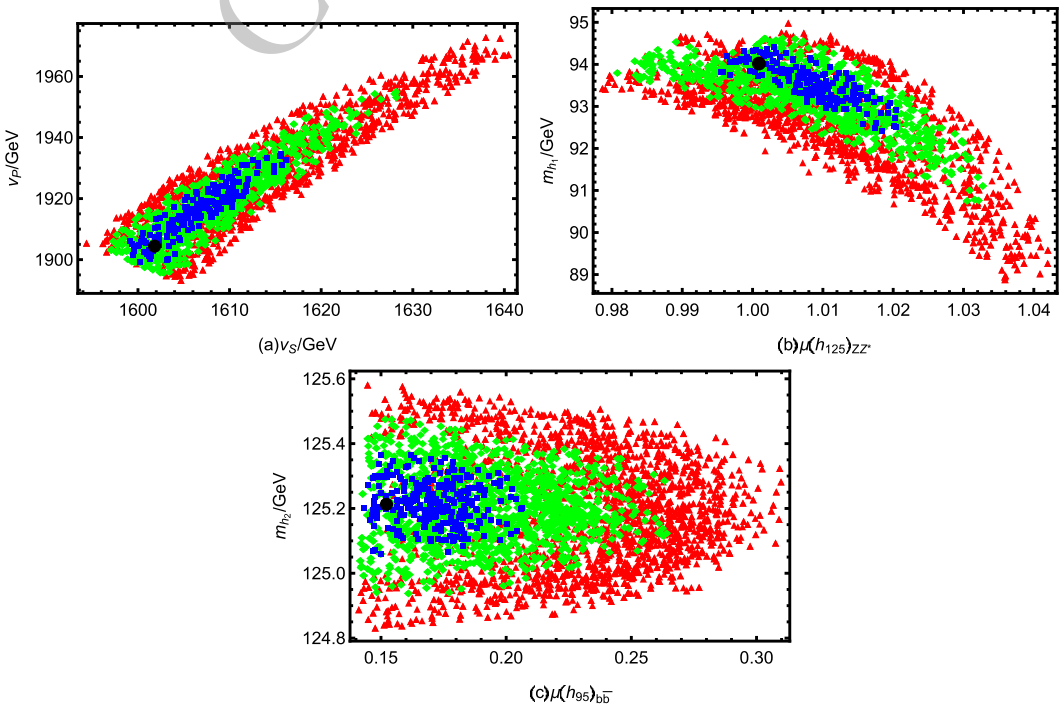

Fig. 4. The symbols denote the χ^2 confidence regions: • marks the best-fit point ($\chi^2_{\text{min}} = 4.39$), ■ the 1σ region ($\chi^2 \le 6.69$), ♦ the 1-2σ region ($6.69 < \chi^2 \le 10.57$), and ▲ the 2-3σ region ($10.57 < \chi^2 \le 16.22$).

Fig. 4(b) depicts the correlation between the Higgs signal strength in the ZZ^* channel and the mass of the lightest scalar, m_{h_1}. The points trace a curved band with a negative slope, in which larger $\mu(h_{125})_{ZZ^*}$ values correspond to smaller m_{h_1}. The best-fit point, $(\mu(h_{125})_{ZZ^*}, m_{h_1}) \simeq (1.00, 94.02\ \text{GeV})$, lies near the densest region. The point distribution reflects the fit quality: points near the center of the band agree better with the data, whereas those farther away correspond to poorer fits along the same trend. Even small deviations of $\mu(h_{125})_{ZZ^*}$ from unity induce noticeable shifts in m_{h_1}, indicating that the light-scalar sector is highly sensitive to precision Higgs measurements.

Fig. 4(c) shows the distribution of points in the $(\mu(h_{95})_{\gamma\gamma}, m_{h_2})$ plane. The values of $\mu(h_{95})_{\gamma\gamma}$ span $0.14 \lesssim \mu(h_{95})_{\gamma\gamma} \lesssim 0.31$, whereas the SM-like Higgs mass is tightly constrained to a narrow window around 125 GeV. The points exhibit a layered structure rather than a uniform spread: a compact ■ core is surrounded by a ♦ band and further enclosed by a ▲ envelope, delineating progressively less-favored regions of parameter space. The global best-fit point is located at $(\mu(h_{95})_{\gamma\gamma}, m_{h_2}) \simeq (0.152, 125.21\ \text{GeV})$, lying within the innermost region. This pattern highlights that the Higgs mass is tightly constrained, in contrast to the greater flexibility of the di-photon rate.

In the $U(1)_X$VLFM, g_X denotes the gauge coupling of the additional $U(1)_X$ symmetry, while the parameter g_{YX} quantifies the gauge mixing between hypercharge $U(1)_Y$ and $U(1)_X$. In Fig. 5, rather than fixing g_X and g_{YX} as in the previous analyses, we allow them to vary over the broader ranges $0.25 < g_X < 0.7$ and $-0.3 < g_{YX} < 0.1$, keeping all other parameters fixed: $Y_{XE} = 0.46$, $Y_{PE} = 0.32$, $Y_{XD} = 0.41$, $Y_{PD} = 0.3$, $Y_{XU} = 0.49$, $Y_{PU} = 0.41$, $v_S = 1600\ \text{GeV}$, and $v_P = 1900\ \text{GeV}$. The resulting point distribution is shown in terms of the χ^2 values, with the best-fit point at $\chi^2_{\min} = 4.41$ (indicated by •). The confidence regions are represented by ■ (1σ, $\chi^2 \le 6.71$), ♦ (1-2σ, $6.71 < \chi^2 \le 10.59$), and ▲ (2-3σ, $10.59 < \chi^2 \le 16.24$).

Fig. 5(a) presents the correlation between g_X and the Higgs signal strength $\mu(h_{125})_{\tau\tau}$. The scanned points form a positively correlated band, indicating that larger g_X generally enhances $\mu(h_{125})_{\tau\tau}$. Fit quality is encoded by color and shape: the most-favored points (■) cluster in the lower-left region of the band, while less-favored points (♦ and ▲) lie farther along the same trend.

Fig. 5(b) plots g_{YX} versus $\mu(h_{125})_{ZZ^*}$. The points lie within a horizontally elongated band with a slight negative slope: those in the 1σ region (■) are concentrated at the lower edge of the band, while the 2σ (♦) and 3σ (▲) regions extend upward. This pattern highlights the sensitivity of $\mu(h_{125})_{ZZ^*}$ to gauge mixing effects.

Fig. 5(c) shows the relationship between the masses of the two CP-even Higgs bosons, m_{h_1} and m_{h_2}. The points are confined to a narrow diagonal strip, consistent with a scenario in which one scalar has a mass near 95 GeV, aligning with the potential excess, while the other corresponds to the observed Higgs boson at 125 GeV. The fit quality is indicated by a color gradient along the diagonal: the blue area encompasses the global best-fit

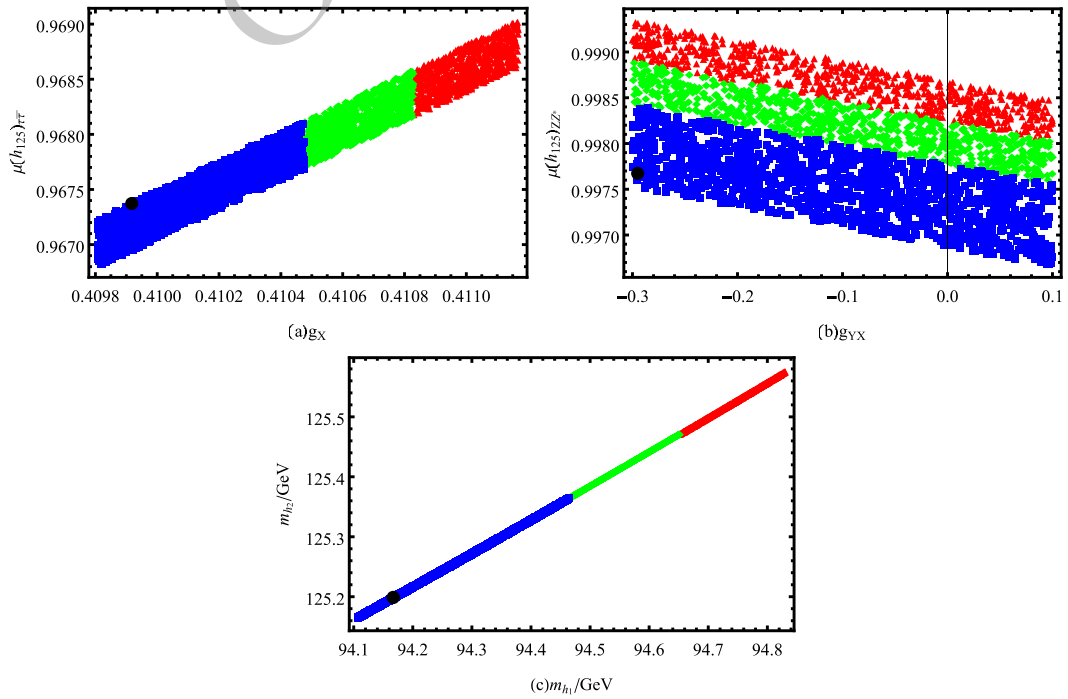

Fig. 5. The symbols denote the χ^2 confidence regions: • marks the best-fit point ($\chi^2_{\min} = 4.41$); ■ the 1σ region ($\chi^2 \le 6.71$); ♦ the 1-2σ region ($6.71 < \chi^2 \le 10.59$); and ▲ the 2-3σ region ($10.59 < \chi^2 \le 16.24$).

point at $(m_{h_1}, m_{h_2}) \simeq (94.17,125.20)$ GeV, suboptimal points appear in green, and poorer fits in red. This blue-to-red gradient clearly illustrates the variation in χ^2 and underscores the excellent agreement of the model predictions with the Higgs data.

In the parameter ranges corresponding to Fig. 4, $v_S = 1200$-2500 GeV and $v_P = 1600$-2800 GeV; in Fig. 5, $g_{YX} = -0.3$-0.1 and $g_X = 0.25$-0.7. Since $\frac{g_{YX}^2}{g_X^2} < 1$, the correction is dominated by the suppression factor $\frac{v^2}{16v_P^2+4v_S^2}$. For the representative parameter choices used in Figs. 4 and 5 ($g_{YX} = -0.1$, $g_X = 0.41$, $v = 246$ GeV, $v_S = 1600$ GeV, $v_P = 1900$ GeV), the correction is at the 10^{-5} level.

VI. DISCUSSION AND CONCLUSION

In this work, we perform a systematic study of the $U(1)_X$ VLFM. The gauge symmetry of this framework is extended to $SU(3)_C \otimes SU(2)_L \otimes U(1)_Y \otimes U(1)_X$. Compared with the SM, the particle content is enlarged by three generations of right-handed neutrinos (ν_R) and two singlet Higgs fields (ϕ and S). In addition, the model introduces one generation of vector-like quarks, a vector-like lepton, and a vector-like neutrino. With significantly fewer free parameters than supersymmetric extensions, the $U(1)_X$ VLFM provides a theoretically consistent and economical framework for exploring new physics (NP) beyond the SM.

In the scalar sector, the CP-even components of one Higgs doublet (H) and two Higgs singlets (ϕ, S) mix to form a 3×3 mass-squared matrix. The lightest eigenstate can account for the 95 GeV excess reported at the LHC, while the second-lightest state requires one-loop corrections to reproduce the observed 125 GeV Higgs mass. Using the Higgs signal strengths measured in the $\gamma\gamma$, ZZ^*, WW^*, $b\bar{b}$, and $\tau\bar{\tau}$ channels by ATLAS and CMS, we perform a numerical fit to the model. Our results show that the predictions of the $U(1)_X$ VLFM framework are in better agreement with the experimental data than those of the SM. Viable parameter points exist within the 1σ confidence level of a χ^2 fit, simultaneously accommodating both the 95 GeV excess and the 125 GeV Higgs boson. The gauge couplings g_X, g_{YX}, the singlet VEVs v_S, v_P, and the new Yukawa couplings $Y_{PD}, Y_{XD}, Y_{PE}, Y_{XE}, Y_{PU}, Y_{XU}$ are found to be tightly constrained and highly sensitive to the fit results.

Furthermore, within the $U(1)_X$ VLFM framework, an inert right-handed neutrino can satisfy constraints from dark-matter direct-detection experiments, and the model may additionally provide a new avenue to address the observed lepton-flavor universality violation at tree level. In future work, we will further investigate the $U(1)_X$ VLFM to determine its viable parameter space.

APPENDIX A: ANALYTIC EXPRESSIONS

Here, we use the down-type quark as an example and present selected analytic expressions for illustration.

$$\begin{aligned}
\frac{\partial V_d}{\partial \phi_H} &= -\frac{3}{16\pi^2}\Big[vY_{d_1}^2 f(Q^2,m_{d_1}^2) + vY_{d_2}^2 f(Q^2,m_{d_2}^2) \\
&\quad + X_1 f(Q^2,m_{d_3}^2) + X_2 f(Q^2,m_{d_4}^2)\Big], \\
\frac{\partial V_d}{\partial \phi_S} &= -\frac{3}{16\pi^2}\Big[X_3 f(Q^2,m_{d_3}^2) + X_4 f(Q^2,m_{d_4}^2)\Big], \\
\frac{\partial V_d}{\partial \phi_P} &= -\frac{3}{16\pi^2}\Big[X_5 f(Q^2,m_{d_3}^2) + X_6 f(Q^2,m_{d_4}^2)\Big],
\end{aligned} \tag{A1}$$

with the auxiliary functions defined as

$$\begin{aligned}
&f(Q^2,m_{d_i}^2) = 2m_{d_i}^2(\log\frac{m_{d_i}^2}{Q^2} - 1), \\
&\Delta = \sqrt{(A-C)^2+4B^2},\ \ Y_{d_1} = \frac{\sqrt{2}m_d}{v},\ \ Y_{d_2} = \frac{\sqrt{2}m_s}{v}, \\
&A = \frac{1}{2}v^2Y_{d_3}^2,\ \ B = \frac{1}{2}vv_SY_{d_3}Y_{XD},\ \ C = \frac{1}{2}v_S^2Y_{XD}^2 + \frac{1}{2}v_P^2Y_{PD}^2, \\
&X_1 = \frac{1}{2}vY_{d_3}^2 - \frac{1}{2\Delta}\Big[(A-C)vY_{d_3}^2 + 2Bv_SY_{d_3}Y_{XD}\Big], \\
&X_2 = \frac{1}{2}vY_{d_3}^2 + \frac{1}{2\Delta}\Big[(A-C)vY_{d_3}^2 + 2Bv_SY_{d_3}Y_{XD}\Big], \\
&X_3 = \frac{1}{2}v_SY_{XD}^2 - \frac{1}{2\Delta}\Big[(C-A)v_SY_{XD}^2 + 2BvY_{d_3}Y_{XD}\Big], \\
&X_4 = \frac{1}{2}v_SY_{XD}^2 + \frac{1}{2\Delta}\Big[(C-A)v_SY_{XD}^2 + 2BvY_{d_3}Y_{XD}\Big], \\
&X_5 = \frac{1}{2}v_PY_{PD}^2 - \frac{1}{2\Delta}\Big[(C-A)v_PY_{PD}^2\Big], \\
&X_6 = \frac{1}{2}v_PY_{PD}^2 + \frac{1}{2\Delta}\Big[(C-A)v_PY_{PD}^2\Big].
\end{aligned} \tag{A2}$$

References

[1] G. Aad, *et al.*, (ATLAS Collaboration), Phys. Lett. B **716**, 1 (2012)

[2] S. Chatrchyan, *et al.*, (CMS Collaboration), Phys. Lett. B **716**, 30 (2012)

[3] G. Aad, *et al.*, (ATLAS and CMS Collaborations), J. High Energy Phys **08**, 045 (2016)

[4] S. Navas, *et al.*, (Particle Data Group), Phys. Rev. D **110**, 030001 (2024)

[5] G. Aad, *et al.*, (ATLAS Collaboration), J. High Energy Phys **07**, 088 (2023)

[6] A. Tumasyanet, *et al.*, (CMS Collaboration), Nature **607**(7917), 60 (2022)

[7] T. Aaltonen, *et al.*, (CDF and D0 Collaborations), Phys. Rev. D **88**(5), 052014 (2013)

[8] G. Aad, *et al*., (ATLAS Collaboration), Eur. Phys. J. C **80**(10), 957 (2020)
[9] G. Aad, *et al*., (ATLAS Collaboration), Eur. Phys. J. C **81**(2), 178 (2021)
[10] G. Aad, *et al*., (ATLAS Collaboration), Eur. Phys. J. C **81**(6), 537 (2021)
[11] M. Aaboud, *et al*., (ATLAS Collaboration), Phys. Rev. D **99**, 072001 (2019)
[12] G. Abbiendi, *et al*., (OPAL Collaboration), Eur. Phys. J. C **27**, 311 (2003)
[13] R. Barate, *et al*., (LEP Working Group for Higgs boson searches, ALEPH, DELPHI, L3 and OPAL Collaborations), Phys. Lett. B **565**, 61 (2003)
[14] S. Schael, *et al*., (ALEPH, DELPHI, L3, OPAL and LEP Working Group for Higgs Boson Searches Collaborations), Eur. Phys. J. C **47**, 547 (2006)
[15] (CDF and D0 Collaborations), arXiv: 1207.0449
[16] (CMS Collaboration), CMS-PAS-HIG-14-037
[17] A. M. Sirunyan, *et al*., (CMS Collaboration), Phys. Lett. B **793**, 320 (2019)
[18] A. M. Sirunyan, *et al*., (CMS Collaboration), J. High Energy Phys **09**, 007 (2018)
[19] (ATLAS Collaboration), ATLAS-CONF-2018-025
[20] A. Tumasyan, *et al*., (CMS Collaboration), J. High Energy Phys **07**, 073 (2023)
[21] G. Aad, *et al*., (ATLAS Collaboration), J. High Energy Phys **07**, 155 (2023)
[22] (CMS Collaboration), CMS-PAS-HIG-20-002
[23] T. Biekötter, S. Heinemeyer, G. Weiglein, Phys. Rev. D **109**(3), 3 (2024)
[24] T. K. Chen, C. W. Chiang, S. Heinemeyer, *et al*., Phys. Rev. D **109**(7), 075043 (2024)
[25] J. J. Cao, X. L. Jia, J. W. Lian, *et al*., Phys. Rev. D **109**(7), 075001 (2024)
[26] J. J. Cao, X. L. Jia, J. W. Lian, Phys. Rev. D **110**(11), 115039 (2024)
[27] T. Biekötter, S. Heinemeyer, G. Weiglein, J. High Energy Phys **08**, 201 (2022)
[28] T. Biekötter, S. Heinemeyer, G. Weiglein, Phys. Lett. B **846**, 138217 (2023)
[29] T. Biekötter, S. Heinemeyer, C. Muoz, Eur. Phys. J. C **78**, 504 (2018)
[30] T. Biekötter, S. Heinemeyer, C. Muoz, Eur. Phys. J. C **79**, 667 (2019)
[31] C. X. Liu, Y. Zhou, X. Y. Zheng, *et al*., Phys. Rev. D **109**, 056001 (2024)
[32] D. Sachdeva, S. Sadhukhan, Phys. Rev. D **101**(5), 055045 (2020)
[33] Z. F. Ge, F. Y. Niu, J. L. Yang, Eur. Phys. J. C **84**, 548 (2024)
[34] M. Aaboud, *et al*., (ATLAS Collaboration), J. High Energy Phys **09**, 001 (2016)
[35] V. Khachatryan, *et al*., (CMS Collaboration), Phys. Lett. B **767**, 147 (2017)
[36] R. Essig, A. Manalaysay, J. Mardon, *et al*., Phys. Rev. Lett **109**, 021301 (2012)
[37] M. Clark, A. Depoian, B. Elshimy, *et al*., Phys. Rev. D **102**(12), 123026 (2020)
[38] J. A. Aguilar-Saavedra, R. Benbrik, S. Heinemeyer, *et al*., Phys. Rev. D **88**(9), 094010 (2013)
[39] J. Cao, L. Meng, L. Shang, *et al*., Phys. Rev. D **106**(5), 055042 (2022)
[40] Q. H. Cao, J. Guo, J. Liu, *et al*., Phys. Rev. D **110**(1), 015029 (2024)
[41] M. E. Peskin, D. V. Schroeder, *An introduction to quantum field theory*, Addison Wesley, Reading, USA, 1995
[42] R. Barate, *et al*., (ALEPH Collaboration), Eur. Phys. J. C **12**, 183 (2000)
[43] P. Abreu, *et al*., (DELPHI Collaboration), Phys. Lett. B **485**, 45 (2000)
[44] S. F. King, S. Moretti, R. Nevzorov, Phys. Rev. D **73**, 035009 (2006)
[45] S. R. Coleman, Phys. Rev. D **7**, 1888 (1973)
[46] J. H. Kang, P. Langacker, T. J. Li, *et al*., J. High Energy Phys **04**, 097 (2011)
[47] B. Yan, T. F. Feng, S. M. Zhao, *et al*., J. Phys. G: Nucl. Part. Phys **48**, 085003 (2021)
[48] C. Anastasiou, K. Melnikov, Nucl. Phys. B **646**, 220 (2002)
[49] J. R. Ellis, M. K. Gaillard, D. V. Nanopoulos, Nucl. Phys. B **106**, 292 (1976)
[50] M. A. Shifman, A. I. Vainshtein, M. B. Voloshin, *et al*., Sov. J. Nucl. Phys **30**, 711 (1979)
[51] A. Djouadi, Phys. Rept **459**, 1 (2008)
[52] J. F. Gunion, H. E. Haber, G. L. Kane, *et al*., Front. Phys **80**, 1 (2000)
[53] M. Carena, I. Low, C. E. M. Wagner, J. High Energy Phys **08**, 060 (2012)
[54] T. F. Feng, S. M. Zhao, H. B. Zhang, *et al*., Nucl. Phys. B **871**, 223 (2013)
[55] W. Y. Keung, W. J. Marciano, Phys. Rev. D **30**, 248 (1984)
[56] J. F. Gunion, H. E. Haber, G. L. Kane, *et al*., *The Higgs Hunter's Guide*, Perseus Books (1990)
[57] P. Gonzalez, S. Palmer, M. Wiebusch, *et al*., Eur. Phys. J. C **73**, 2367 (2013)
[58] W. Bernreuther, P. Gonzalez, M. Wiebusch, Eur. Phys. J. C **69**, 31 (2010)
[59] L. Resnick, M. K. Sundaresan, P. J. S. Watson, Phys. Rev. D **8**, 172 (1973)
[60] J. F. Gunion, H. E. Haber, Nucl. Phys. B **272**, 1 (1986)
[61] A. Arbey, A. Deandrea, F. Mahmoudi, A. Tarhini, Phys. Rev. D **87**, 115020 (2013)
[62] R. Benbrik, M. Boukidi, M. Ech-chaouy, *et al*., J. High Energy Phys **03**, 020 (2025)
[63] V. Chekhovsky, *et al*. (CMS Collaboration), J. High Energy Phys **08**, 156 (2025)
[64] G. Aad, *et al*. (ATLAS Collaboration), Eur. Phys. J. C **85**(11), 1335 (2025)
[65] F. Z. Xu, W. Zhang, J. Li, *et al*., Phys. Rev. D **98**(11), 115033 (2018)
[66] S. Q. Dinh, H. M. Tran, Nucl. Phys. B **997**, 116384 (2023)